New Numerically Derived Scaling Relationships for Impact Basins on Mars

Hely C. Branco[1] [iD], Katarina Miljkovic[1] [iD], and Ana-Catalina Plesa[2] [iD]

[1]School of Earth and Planetary Science, Space Science and Technology Centre, Curtin University, Perth, WA, Australia, [2]German Aerospace Center (DLR), Berlin, Germany

Abstract Most impact basins are believed to have formed during the early epochs of planetary evolution. The planet's gravity, internal structure, and thermal regime have the strongest control over their formation. Because of this, we can use the geophysical constraints on Mars' interior composition, structure, and geophysical evolution derived from the InSight mission to better understand the formation of impact basins on the planet. To achieve this, we performed numerical simulations of large impacts using the iSALE shock physics code. We investigated the effects of temperature and crustal thickness variations on impact basin size and morphology. Our scaling relationships indicate that: (a) basins formed in a warmer crust have larger final diameters in comparison to basins formed in a colder crust, a difference that is further accentuated as basin size gets bigger; and (b) the largest impact basins on Mars were created by impactors ranging from 35 to 680 km in diameter, up to ~32% larger than estimates based on classical scaling. Our results expand the current understanding of the extent of early and large impact bombardment on Mars and provide a more comprehensive knowledge of impact basin formation on planetary surfaces.

Plain Language Summary The recent advancements in the understanding of Mars' that resulted from the InSight mission can be used to better understand the early large bombardment that took place 4.4 to 3.7 Ga ago. This bombardment formed impact basins, the largest and most complex type of craters. Their size and shape depend on the interior structure and temperature of the planet when they formed. We can better understand basins by simulating their formation and comparing the results with observations. Here, we used advanced interior structure and temperature evolution models of Mars to simulate the formation of impact basins as accurately as possible. We simulated basins of various sizes forming at different locations at multiple stages during Mars' evolution. Based on that, we derived equations referred to as scaling relationships that express the connection between basin size and impact conditions for different epochs and locations on Mars. We concluded that: (a) basins formed in a warmer crust are larger than basins formed in a colder crust, and (b) the largest reported basins on the planet were created by impactors much larger than previously thought. Our results provide a more comprehensive knowledge of impact basin formation and valuable insights into the early large bombardment.

1. Introduction

Impact cratering is a common geological process in the Solar System, having played a major role in the formation and evolution of most planetary objects with solid surfaces (Melosh, 1989, 2011). It results in the formation of impact craters exhibiting varying morphologies that mainly depend on the impact energy and geological properties of the target at the time of impact, namely the interior structure, composition, surface gravity, and thermal regime (Melosh, 2011; Osinski & Pierazzo, 2013). Impact basins, the largest of their kind, formed exclusively during the early stages of planetary evolution, mostly within the first billion years following accretion.

Our current understanding of shock physics modeling allows us to simulate the formation of impact craters with high fidelity (e.g., Collins et al., 2004; Ivanov et al., 2010; Trowbridge, 2020). Through comparison of numerical impact cratering simulations with available space exploration data, remote observations, and geophysical modeling at impact crater sites, it is possible to estimate some properties of the target body at the time of crater formation. When applied to a range of similar-sized structures in different localities, it can highlight differences in target properties across different locations (Miljkovic et al., 2013). When applied to similar-sized structures of different ages, it can show how the target properties changed throughout time, deepening the understanding of planetary evolution. Lastly, when applied to a range of crater sizes formed approximately at the same time and

location, it showcases how different crater properties change with size, defining scaling relationships for the target (Miljkovic et al., 2016). Significant progress has been made in understanding impact basins in recent years, with most efforts aimed at the Moon where basins are best preserved (e.g., Johnson et al., 2016, 2021; Miljkovic et al., 2013, 2015, 2016, 2021; Melosh et al., 2013; Potter, 2015; Potter, Collins, et al., 2012, Potter, Kring, et al., 2012). Some of the studies derived scaling relationships between impact conditions and observed crater properties as a function of size. These relationships are critical in describing basin formation and evolution given that the scaling derived from numerical modeling diverges from the semi-empirically derived classical scaling relationships, such as the Π group scaling (Melosh, 1989). For lunar basins, it was demonstrated that the thermal gradients/profiles played the dominant role in final basin size and morphology (e.g., Miljkovic et al., 2016; Potter, Collins, et al., 2012, Potter, Kring, et al., 2012).

Here, we applied similar methodologies made for lunar basins to impact basins on Mars. We used the recent internal structure and thermal evolution models suitable for the basin-forming epoch to simulate large impacts on Mars. We investigated the effects of temperature and crustal thickness variations on basin size and morphology. Based on our simulations, we derived new scaling relationships for impact basins on Mars. We used our scaling to estimate the impactor sizes that formed the observed impact basins on Mars and compared our results to the predictions made by Π group scaling (Melosh, 1989). We also discussed the target properties that play the largest role in the basin formation on Mars, and their effects on final basin size and morphology. We concluded that the target properties play the largest role in basin formation on Mars. Our extensive range of simulations provided a database with a comprehensive knowledge of impact basin formation on Mars and insight into the extent of large impact bombardment in the early stages of the planet's evolution.

2. Hydrocode Simulation Setup

We performed numerical simulations of impact basins on Mars using the iSALE-2D Dellen for Python 3 release of iSALE, a multi-material, multi-rheology shock physics code that can simulate impact cratering in geological materials. It is an extension of the Simplified Arbitrary Lagrangian Eulerian hydrocode (Amsden et al., 1980), including many extensions, corrections, and enhancements from various workers such as elasto-plastic constitutive models, fragmentation models, equations of state for various materials, modified strength models, and a dilatancy model (e.g., Collins, 2014; Collins et al., 2004, 2011; Ivanov et al., 1997; Melosh et al., 1992; Wünnemann et al., 2006). On Mars, impact basins have diameters larger than ~90 km (Baker, 2016). In this study, we focused on basins with diameters from ~200 to ~1,400 km, as impacts within this size range likely probe both crust and mantle while being mostly unaffected by the planet's curvature.

Our assumptions regarding Mars' crust and mantle properties were based on the latest interpretations of the interior structure of Mars derived from the Interior Exploration using Seismic Investigations, Geodesy and Heat Transport (InSight) mission led by NASA (e.g., Golombek et al., 2020; Johnson et al., 2020; Knapmeyer-Endrun et al., 2021; Lognonné et al., 2020; Stähler et al., 2021). These interpretations were built upon in situ seismic measurements and represent the most accurate models of Mars' interior structure to date. The planet's crust formed early and is believed to be mostly made of basaltic rocks associated with low degrees of partial melting (Groot et al., 2013). Based on the seismic measurements performed by InSight and on the analysis of gravity and topography data, the average thickness of the Martian crust (ct) lies between 30 and 72 km, while crustal thickness variations range from less than 5 km at the center of large impact basins such as Hellas and Isidis to more than 120 km in certain regions of the southern highlands (Wieczorek et al., 2022). Seismic discontinuities were identified beneath the InSight lander at ~8 and ~20 km depths, indicating a two- or three-layer crustal structure (Knapmeyer-Endrun et al., 2021; Li et al., 2022). The crustal layering was suggested to have started to form after the initial stages of crustal evolution on Mars, possibly after the formation of the impact basins (Wieczorek et al., 2022). Hence, here we assume that the crust on early Mars can be represented by a single basalt layer. We considered two crustal thickness values, 47 km (thin crust) and 91 km (thick crust), roughly corresponding to the average crustal thickness for the northern lowlands and the southern highlands (Plesa et al., 2022).

A few attempts at dating impact basins on Mars have been made (e.g., Farley et al., 2013; Frey, 2008; Marchi, 2021; Robbins et al., 2013; Werner, 2008, 2014, 2019; Werner et al., 2011). According to these studies, basins on Mars have ages ranging from 3.4 to 4.3 Ga. The ages attributed to Mars' basins often vary tens to hundreds of Ma between studies. Argyre basin, for example, has attributed ages of 4.04 (Frey, 2008), 3.93 (Robbins et al., 2013) and 3.83 (Werner, 2008) Ga, a variation at best of 0.1 Ga (100 Ma) and at worst of 0.21 Ga (210 Ma). This is a substantial
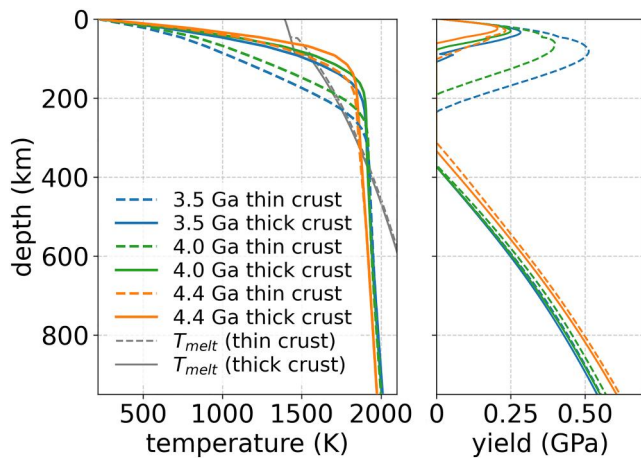
Figure 1. Temperature (left) and associated yield strength profiles (right) used in our numerical simulations of impact basins on Mars. They were calculated at 4.4 Ga (orange) when the crust was comparatively hotter, 4.0 Ga (green) when the crust was in an intermediate state, and 3.5 Ga (blue) when the crust was comparatively colder (blue). We considered two crustal thickness values, thin (47 km, dashed lines) and thick (91 km, solid lines), corresponding to the average crustal thicknesses of the northern lowlands and the southern highlands. The solidus temperature profiles (T_{melt}) assumed by iSALE are shown in gray. The abrupt change in the solidus comes from the transition from a basaltic crust to a dunitic mantle.

difference, especially when considering the significant variations in the planet's thermal state during the first hundreds of Ma from accretion (Plesa et al., 2022). To account for this variability, we considered a wide range of ages in our modeling. We adopted the temperature profiles appropriate for the early stages of Mars' thermal evolution from Plesa et al. (2022). These profiles result from the most up-to-date global geodynamic models that consider the internal structure of Mars (i.e., core size, crustal thickness, and crustal thickness variations) as derived from InSight data. Such models are a powerful tool for estimating the thermal state of the Martian interior throughout the planetary history by using available geological, geochemical, and geophysical constraints (Plesa et al., 2018). We chose three points in time to focus our analysis: at 4.4 Ga, when the crust was relatively hot, at 4.0 Ga, an intermediate state, and at 3.5 Ga, when the crust was comparatively colder. Hence, we selected six different temperature profiles which were used as inputs for our simulations (Figure 1). All temperature profiles crossed the melting temperature (T_{melt}) calculated by iSALE, resulting in distinct yield strength variations with depth.

The target was considered flat, composed of a basaltic crust and a dunitic mantle, and had a surface temperature of 213 K. We considered spherical projectiles traveling at 10 km/s, the average speed of impacts on Mars (Ivanov, 2008). Ten projectile sizes were tested, from 20 to 200 km in diameter spaced in 20 km increments, producing 40 impact basins ranging from ∼200 to ∼1,700 km in main rim diameter. We used the basalt and dunite equations of state originally proposed by Thompson and Lauson (1972) and later updated by Melosh (1989), the damage model proposed by Ivanov et al. (1997), the thermal softening model proposed by Ohnaka (1995), and the simplified acoustic fluidization model (or "block model") proposed by Melosh (1997). No porosity model was used as it was deemed insignificant in lunar basin simulations (Miljkovic et al., 2013). All input parameters, material models, iSALE impact and material input files, and measurements are available in our online repository available at doi.org/10.5281/zenodo.10100099 (Branco et al., 2023).

We considered vertical impacts (i.e., impact angle of 90° measured from the horizontal) in cylindrical symmetry, with a vertical symmetry axis along the direction of impact. In this setting, impacts are simulated as 2D vertical cross sections of half-craters. The coordinate system is centered at the point of contact between the projectile and the surface of the target. Crater size was measured radially along the pre-impact surface level (0 km elevation) from the point of impact (Figure 2). A cylindrical symmetry axis demands free slip, which can result in over-estimation of material motion along it. Thus, fluctuations in cells along the symmetry axis could be disregarded if the majority of the craters stopped moving within a reasonable time interval. Henceforward, we considered that the crater finished forming once there was no significant material movement over 5 computational cycles at a distance equivalent to more than 10 numerical cells from the symmetry axis.
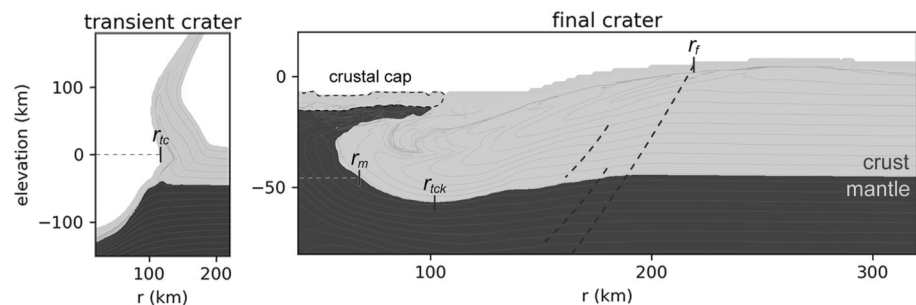
Figure 2. Example of cross sections of a half crater for the transient crater (left) and the final crater (right) used for our measurements of transient crater radius (r_{tc}) and final crater radius (r_f). Inferred faults (dashed black lines), crustal cap (finely dashed black line), radius of mantle uplift (r_m) and radius of crustal thickening (r_{tck}) are also shown. The basin was made by a 60 km in diameter dunite impactor traveling at 10 km/s, hitting a flat target composed of a 47 km thick basaltic crust overlaying a dunitic mantle at 3.5 Ga. This resulted in a crater of $r_{tc} = 137$ km and $r_f = 210$ km.

Sufficiently large impacts at moderate impact angles form craters with approximately circular planforms. Progressively shallower impact angles result in increasingly asymmetric inner crater structures without significantly changing the overall crater profile (Collins et al., 2020). Hence, for the intent of this work, variations in impact angle were assumed to have mostly affected the magnitude of the vertical component of the impact velocity vector. Crater formation depends on impact energy and momentum, in which mass and speed are difficult to decouple. Statistically speaking, impacts most likely occur at approximately 45° (Pierazzo & Melosh, 2000). A vertical impact of 10 km/s represents a range of oblique impacts at higher. From this perspective, our simulations represent the upper range of speeds expected for impacts on Mars (Le Feuvre & Wieczorek, 2011). Therefore, impactor size estimates based on our simulations can be considered a lower bond, as slower impactors would need to be more massive to form impact basins of the same size.

The cells per projectile radius value define the numerical resolution of an iSALE simulation. We used 20 CPPRs, which provide consistent results in the basin morphology overall independent of the numerical cell size (e.g., Miljkovic et al., 2013). The physical size of each cell ranged from 0.5 by 0.5 km for the smallest impacts to 5 by 5 km for the largest. The numerical mesh size ranged from 430 by 430 cells for the smallest impacts to 560 by 560 for the largest.

We used cross-sections of half craters showing the crust, mantle, and material tracers for our measurements (Figure 2). We first analyzed the transient crater (left panel). In larger impact basins, excavation doesn't end contemporaneously in all directions. Instead, crater collapse in the form of crater floor uplift begins prior to the transient cavity reaching its maximum lateral extent (Potter, 2011). Because of that, we measured the transient crater radius (r_{tc}) as the radius of the transient cavity at 0 km elevation at the moment of maximum excavated volume. We also analyzed the final impact crater (right panel) formed once most of the material stabilized and stopped moving. The final crater cross sections generally included an area of crustal thinning and mantle uplift at the crater center, followed by an area of crustal thickening further away from the impact point. We considered the final crater radius (r_f) as the main rim radius. The main rim was defined at the surface expression of the main fault, that is, the structure indicated by tracer displacements formed during crater collapse that crosscut both crust and mantle and remained identifiable until the end of the simulation.

3. Target Effects on Final Crater Morphology

For the same impact conditions, different temperature profiles and crustal thickness combinations resulted in significant changes in the final crater morphology. The differences can be evident throughout the entire size range considered in this study. An example in Figure 3 shows an impact basin made by a 60 km in diameter dunite impactor hitting a flat target composed of a basaltic crust overlaying a dunitic mantle at 10 km/s. We considered two crustal thickness values, 47 km (thin crust, left column) and 91 km (thick crust, right column), and three points in time, 3.5 Ga (top panels), 4.0 Ga (middle panels) and 4.4 Ga (bottom panels), forming craters with the final diameter between 210 and 240 km. The 3.5 Ga and 4.4 Ga cases in the presence of the end member cases for the youngest and oldest crust during the basin-forming epoch.

Impact basins formed in a thin crust (Figure 3, left column) at different ages presented distinct morphologies. Basins that formed in a thin crust at 3.5 Ga showed a discernible main rim marked by a topographical high aligned with faults marked by a near-vertical displacement of tracer lines. A crustal cap was present, covering the uplifted mantle in a patchy manner. The radius of mantle uplift (r_m) comprised 15%–20% of the final basin radius. The radius of crustal thickening (r_{tck}) was equivalent to 50% of the final basin radius. An impact basin formed in a thin crust at 4.0 Ga also presented a topographical high aligned with faults, however less pronounced. It also presented a crustal cap covering, at least partially, the uplifted mantle. The values of r_m and r_{tck} were equivalent to 35%–40% and 75%–80% of the final basin radius, respectively, both larger than those observed in basins formed in a thin crust at 3.5 Ga. Basin formed in a thin crust at 4.4 Ga was different from the younger cases. No distinct topographical features were observed. The radius of crustal thickening approximately coincided with the final radius ($r_{tck} \approx r_f$) and the value of r_m was equivalent to 60%–70% of the final basin radius, much larger than the values observed in basins formed in a thin crust at 3.5 and 4.0 Ga.

Impact basins that formed in a thick crust (Figure 3, right column) presented the same overall behavior. The topographical profile was mostly flat with no prominent topographical features. The radius of crustal thickening was ~10% larger than the final basin radius. The radius of mantle uplift was equivalent to ~50% of the final basin radius. Lastly, mixing between heated crustal and mantle material was observed at the crater center. The amount
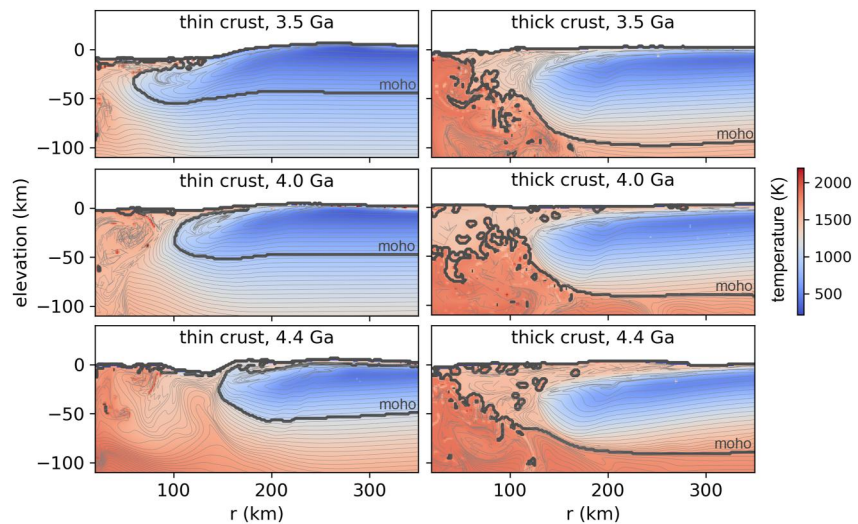
Figure 3. Example of impact simulations made with iSALE2D, shown as vertical cross-section of half craters. The basins result from a 60 km in diameter dunite impactor hitting a flat target composed of a basaltic crust and a dunitic mantle at 10 km/s. We considered two crustal thicknesses, 47 km (thin crust, left column) and 91 km (thick crust, right column), and three points in time, 3.5 (top panels), 4.0 (middle panels), and 4.4 Ga (bottom panels), making craters with the final diameter r_f between 210 and 240 km. The dark gray lines represent the topographical profiles of the final crater and the crust-mantle interfaces (moho). Colored contours represent the temperature approximately 1 hr after impact.

of mixing varied with age, being the smallest in volume for impact basins formed at 3.5 Ga and largest in basins formed at 4.4 Ga.

The areas of the highest temperatures observed in basins approximately 1 hour after impact can be used to infer melt formation (Figure 3). In this study, we do not address the specifics of melt generation, as melt volumes in impact basins on Mars were detailed in previous works (e.g., Manske et al., 2021). Instead, we offer a simple observation that the amount of inferred melt varied with age and crustal thickness. Basins formed in the hottest scenario (i.e., thick crust at 4.4 Ga) presented the largest volume of melt, while craters formed in the coldest scenario (i.e., thin crust at 3.5 Ga) presented the smallest.

4. Classical Scaling Relationships

One of the most commonly used forms of evaluating the relationship between impact conditions and the resulting crater is the Π group scaling relationship. Originally devised by Buckingham (1914) and further elaborated by Bridgman (1949), it can be interpreted as a detailed form of dimensional analysis in which the functional dependence of the most relevant physical parameters associated with the impact cratering process is analyzed (Melosh, 1989). In the following section, we give a summary based on the formulation presented by Melosh (1989, 2011). For the interested reader, a more extended formulation is available in Holsapple and Schmidt (1982) and Holsapple (1987, 1993).

For sufficiently large impact structures, the crater forming process is dominated by gravity. Assuming vertical impacts on this setting, two dimensionless parameters π_i that correlate most relevant impactor and target variables are defined by the following equations:

$$\pi_D = D_{tc}\left(\frac{\rho_t}{m}\right)^{\frac{1}{3}} \tag{1}$$

$$\pi_2 = \frac{1.61gL}{v_i^2} \tag{2}$$

where D_{tc} is the transient cavity diameter, ρ_t the target density, m the projectile mass, L the projectile size, v_i the impact velocity, and g the surface gravity acceleration of the target (Melosh, 1989). For Mars, $g = 3.721$ m/s^2

(Hirt et al., 2012). If we assume a spherical projectile with the same density as the target, then $\pi_D = f(\pi_2)$, which was experimentally shown to be equivalent to

$$\pi_D = C_D \pi_2^{-\beta} \tag{3}$$

where C_D and β are experimentally derived constants that vary according to the target material. For example, for water $C_D = 1.88$ and $\beta = 0.22$, for quartz sand $C_D = 1.4$ and $\beta = 0.16$, and for saturated rock/soil $C_D = 1.6$ and $\beta = 0.22$. In other words, Equation 3 can be seen as a mathematical description of material behavior, and π_D vs π_2 plots can be used as a visual demonstration of the differences between different materials, which are plotted as distinct lines. It can be rewritten as

$$D_{tc} = C_D\, 1.61^{-\beta}\left(\frac{\pi}{6}\right)^{\frac{1}{3}} g^{-\beta}\, v_i^{2\beta}\, L^{(1-\beta)} \tag{4}$$

which corresponds to the scaling for craters forming in competent rock in the gravity domain (Melosh, 2011), assuming C_D and β for saturated rock/soil. For impacts on Mars at $v_i = 10$ km/s, Equation 4 becomes:

$$D_{tc} = 50.05\, L^{0.78} \tag{5}$$

which can be rewritten in terms of radii as

$$r_{tc} = 25.03\, L^{0.78} \tag{6}$$

There are different conversions between the transient crater diameter (D_{tc}) and the final crater diameter (D_f). These conversions are derived experimentally, and depend on crater size and target materials, being the most uncertain for larger craters/basins (Melosh, 1989, 2011). One example is

$$D_f = 1.17 \frac{D_{tc}^{1.13}}{D_{sc}^{0.13}} \tag{7}$$

where D_f is the final crater diameter and D_{sc} is the transition diameter between simple and complex craters (Melosh, 2011). On Mars, $D_{sc} = 6$ km (Robbins & Hynek, 2012). Equation 7 can also be rewritten in terms of radii, resulting in the following equation:

$$r_f = 0.41\, r_{tc}^{1.13} \tag{8}$$

Lastly, Equations 6 and 8 can be combined, resulting in the following equation:

$$r_f = 15.28\, L^{0.88} \tag{9}$$

Equations 6, 8, and 9 are power laws of the general form $y = ax^b$, where a and b are constants, and can be easily compared to power law fits derived from our simulations. Hence, we evaluated the relationship between our measurements of r_{tc}, r_f and L and derived scaling relationships of the types $r_{tc} = f(L)$, $r_f = f(L)$ and $r_f = f(r_{tc})$.

We used Equations 1 and 2 to calculate π_D and π_2 values for our r_{tc} measurements (Figure 4) and compared our results (colored markers) with the Π group scaling relationship for standard materials (dashed lines). No discernible trend was observed for basins with $r_f < 400$ km. For larger basins, the overall behavior roughly approximated that of consolidated rock/soil (gray dashed line). For a given crater size (or π_2 value), basins formed in a thick crust presented mostly the same behavior, with π_D values higher than those expected for consolidated rock/soil. Basins formed in a thin crust varied significantly with age. Impacts at 4.4 Ga resulted in basins with overall behavior matching consolidated rock/soil. Impacts at 4.0 and 3.5 Ga resulted in lower π_D values, often smaller than the expected values for consolidated rock/soil. The great variance in overall behavior across the different scenarios considered in this study indicates that comparisons between π_i parameters from the Π group scaling are not sufficient for the understanding of basin formation on Mars, requiring more elaborate approaches.
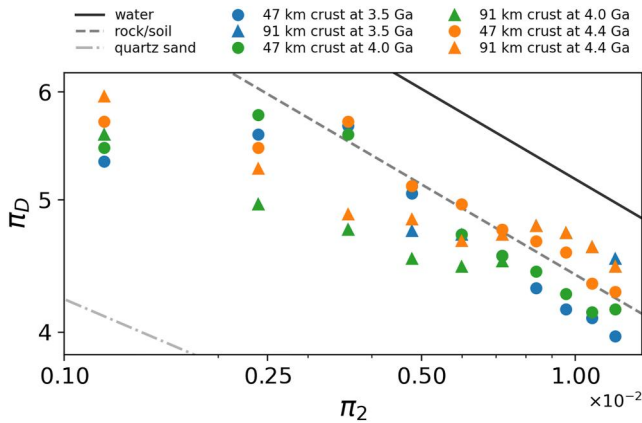
Figure 4. Π group scaling relationship for water (solid line in black), consolidated rock/soil (dashed line in dark gray) and quartz sand (dash-dot line in light gray). The colored markers correspond to individual measurements made from our simulations calculated using Equations 1 and 2, color coded according to age: blue for 3.5 Ga, green for 4.0 Ga, and orange for 4.4 Ga. Two crustal thicknesses were considered: 47 km (thin crust, circular markers) and 91 km (thick crust, triangular markers). Crater size increases toward the bottom right corner of the plot.

5. New Numerically Derived Scaling Relationships for Mars' Basins

For most ages and crustal thicknesses investigated, the Π group scaling (Equation 4) slightly underestimated r_{tc} for craters smaller than 200 km and overestimated it for craters larger than 200 km (Figure 5a). There were two exceptions to this generalization. For a thin young crust (47 km at 3.5 Ga), Π group scaling overestimated r_{tc} for the entire size range. For a thin intermediate crust (47 km at 4.0 Ga), Π group scaling agreed with our scaling for craters larger than 100 km. The differences between the Π group scaling and our numerically derived scaling increased with basin size. Differences start at ~5% for smaller basins, decreasing until eventually getting into agreement with Π scaling for r_{tc} = 200 km and increasing for larger basins, reaching ~10% for the largest size considered in this study.

There were significant differences between Π group scaling (Equation 9) and the $r_f = f(L)$ numerically derived scaling (Figure 5b). Overall, the Π group scaling better agreed with our numerically derived scaling for a thick crust (91 km) and diverged more from our scaling for a thin crust (47 km). For craters with r_f smaller than 200 km formed in thin crust, the Π group scaling reasonably agreed with the numerically derived scaling. In all other scenarios, it overestimated r_f, with differences increasing with size. Differences range from ~5% for smaller basins, reaching ~20% for the largest basin considered in this study.

The differences were also noticeable when comparing the Π group scaling (Equation 8) with the $r_f = f(r_{tc})$ numerically derived scaling (Figure 5c). Overall, our new scaling predicts that, for a given r_f, basins will have larger r_{tc}. Differences in relation to Π group scaling start at ~5% for smaller basins, decreasing until eventually getting into agreement classical scaling for r_f = 250 km and increasing for larger basins, exceeding 20% for the largest size considered in this study. Similar to the other scenarios, this tendency becomes more prominent as crater size increases, and is affected by crustal thickness and age. For a given r_f, basins formed in a young thin crust present lower r_{tc}, while craters formed in old thick crust present higher r_{tc} values, with differences not exceeding 10% between scenarios.

In summary, our new scaling was derived considering the effects of the thermal evolution within the first billion years on Mars and the most recent estimates of the planet's crustal thickness thanks to the NASA InSight mission and associated modeling. Our scaling is best suited for impact basins with main rim radius larger than 100 km, being particularly relevant for basins larger than 250 km in main rim radius, a scale in which divergences with

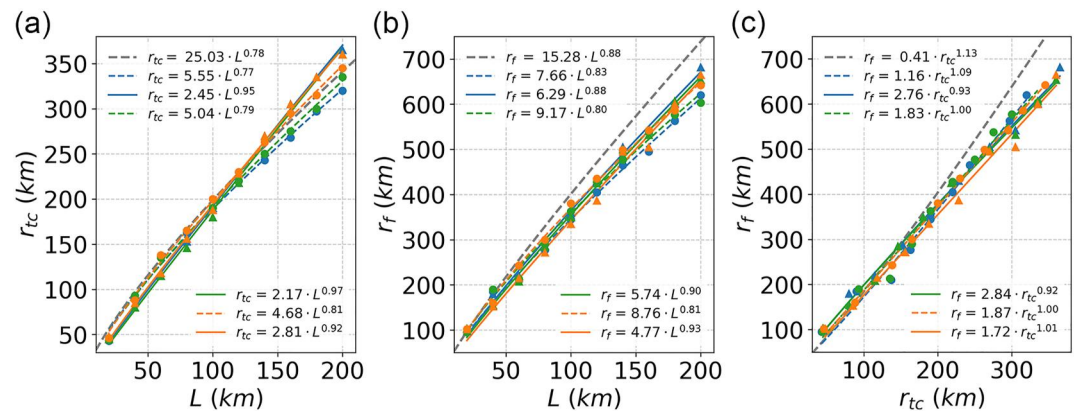**Figure 5.** (a) $r_{tc} = f(L)$, (b) $r_f = f(L)$, and (c) $r_f = f(r_{tc})$ scaling relationships for Mars basins, where r_{tc} is the radius of the transient crater, L is the impactor diameter, and r_f is the final basin radius. The colored markers correspond to radii measurements for the six target cases; color coded the same as in Figure 1. The gray line corresponds to the Π group scaling as defined by Equations 6, 8 and 9.

classical scaling, namely Π group scaling, become more apparent. For basins with a final radius smaller than 250 km, our scaling is mostly in agreement with Π group scaling. For larger basins, our scaling predicts larger transient craters and smaller final crater radii than Π group scaling. The discrepancy grows as the basin size increases for all scenarios considered in this study. This has implications in inferring the extent of impact bombardment on early Mars, as it will be detailed in the following sections.

6. Impactor Size and Transient Crater Radii Estimates for Impact Basins on Mars

We used our numerically derived scaling relationships to estimate impactor size (L) and transient crater radius (r_{tc}) of the largest impact basins on Mars. We adapted the impact basin list from Lillis et al. (2013), which includes a total of 41 craters from 150 to 1,700 km in radius formed between ~4.2 and ~3.8 Ga (Table 1). We used the reported final basin radius ($r_{f(lit)}$) to estimate L and r_{tc} using our scaling relationships. Favored values were chosen based on the best correspondence between a crater's age and average surrounding crustal thickness (ct) to the six scenarios considered in our study. We verified if the average crustal thickness better approximated a thin or thick crust based on the colored crustal thickness map available in JMARS (Goossens et al., 2017; Table S1). For example, Huygens crater formed either at 3.8 (Werner, 2008) or at 4.0 Ga (Robbins et al., 2013) in a terrain with average crustal thickness of ~50 km, better corresponding to our scaling for thin crust at 4.0 Ga. A full list of values (numerical and observational) is available in the supplementary materials (Table S1).

According to our scaling, the impact basins listed in Table 1 were created by impactors ranging from 35 to 680 km in diameter (L). It differs from impactor size estimates from Π group scaling (L_{ss}), which predict diameters from 32 to 510 km for the same impact speed and angle. For the entire size range considered in this study, our scaling predicts larger projectiles for each given basin in comparison to Π group scaling, with differences as high as 32% in impactor diameter (Figure 6a). Transient crater radius estimates based on our scaling (r_{tc}) also diverge from estimates based on Π group scaling ($r_{tc(ss)}$) in all cases (Figure 6b). Values of $r_{tc(ss)}$ presented differences up to 40%. For basins with a final diameter smaller than 170 km, Π group scaling predicts larger transient crater radii than our scaling. For basins with larger final diameters, our scaling predicts larger transient crater radii. Discrepancies grow with the increasing crater size.

The distribution of impactor sizes (Figure 7a) estimated by our scaling relationships indicates that most impactors are smaller than 300 km in diameter. There are two distinct frequency peaks centered at 40 and 180 km, while the second peak is wider. The distribution for Π group scaling also indicates that most impactors are smaller than 300 km, presenting two distinct frequency peaks at 40 and 140 km, while the second peak is also wider. The kernel density distribution (KDE) of impactor sizes for both types of scaling relationships is reasonably similar, with one prominent peak centered around 160 km (Figure 7b). The KDE based on our simulations is wider than the KDE based on Π group scaling, reflecting the narrower range of impactor sizes predicted by Π group scaling in comparison to our scaling.

7. Temperature Effects on Basin Size and Morphology on Mars

The scaling relationships derived from our simulations show that the size and morphology of impact basins on Mars are controlled by age (thermal conditions in the interior) and crustal thickness. For the same impact conditions and crustal thickness, craters formed at 3.5 Ga (young crust) tend to be smaller than craters formed at 4.4 Ga (old crust). Similarly, craters formed in a thin crust (47 km) tend to be smaller than craters formed in a thick crust (91 km). Overall, there are significant differences in the final basin morphology, with a comparatively less mantle uplift and a more prominent crustal thickening observed in younger basins formed in a thin crust compared to older basins formed in a thick crust.

In this work, we investigated crustal thickness and temperature effects as separate target parameters. Both age and crustal thickness variations imply different temperature profiles. There is a dependence between temperature and age, that is, old crust (4.4 Ga) is warmer than young crust (3.5 Ga). At the same time, a thicker crust is associated with a higher amount of heat producing elements and a pronounced blanketing effect that leads to a warmer lithosphere (Knapmeyer-Endrun et al., 2021). Consequently, for a given age, higher crustal thickness values imply higher overall temperatures. This was also visible in the temperature profiles assumed in this study. Figure 1 shows that temperature profiles for older geological past have higher average temperatures and steeper temperature gradients than temperature profiles calculated for more recent geological epochs. Similarly, temperature profiles calculated for a thicker crust have larger average temperatures and steeper temperature gradients

Table 1
Impactor Size (L) and Transient Crater Radius (r_{tc}) Estimates for Mars Largest Basins

Name	Long	Lat	$r_{f(lit)}$	ct	age[1]	age[2]	age[3]	r_{tc}	L	$r_{tc(ss)}$	L_{ss}
Utopia	115.5	45.0	1690	thin	4.11	–	–	923.50	679.04	709.72	511.39
Ares	343.9	4.0	1650	thin	4.17	–	–	901.64	659.01	694.83	497.68
Acidalia	342.7	59.8	1543.5	thin	4.13	–	–	843.44	606.28	654.99	461.40
CT3-D	166.0	−41.2	1442	thin	4.18	–	–	787.98	556.86	616.73	427.13
Amazonis	187.9	27.1	1436.5	thin	4.15	–	–	784.97	554.20	614.65	425.28
Daedalia	228.3	−26.4	1319.5	thick	4.20	–	–	792.52	420.62	570.13	386.20
North Polar	197.0	80.4	1072.5	thin	4.12	–	–	586.07	384.62	474.59	305.27
Hellas	66.4	−42.2	1035	thin	4.07	4.02	3.99	565.57	367.89	459.87	293.19
Solis	275.7	−25.4	882	thick	4.15	–	–	511.52	268.85	399.17	244.53
Chryse	318.0	25.0	862.5	thin	4.14	–	–	471.31	292.91	391.35	238.41
CT3-F	140.8	−0.2	790	thin	4.16	–	–	431.69	262.47	362.09	215.80
CT3-H	7.9	28.5	717	thin	4.25	–	–	383.42	230.01	332.32	193.32
SE Elysium	170.3	3.7	701.5	thick	4.13	–	–	398.81	208.46	325.95	188.59
Isidis	87.8	13.4	676	thin	–	3.97	3.96	369.40	216.01	315.45	180.83
North Tharsis	243.6	17.6	673.5	thick	4.14	–	–	381.54	199.23	314.41	180.07
Argyre	317.5	−48.9	657.5	thin	4.04	3.93	3.83	359.29	208.65	307.80	175.22
CT3-C	138.8	−72.1	640	thick	4.24	–	–	350.91	194.00	300.53	169.94
SW Daedalia	213.9	−29.3	639	thick	4.18	–	–	360.35	187.93	300.12	169.64
CT3-G	36.5	−2.2	622.5	thin	4.18	–	–	340.16	194.86	293.25	164.68
Zephyria	164.3	−12.3	596.5	thin	4.21	–	–	318.98	183.27	282.38	156.90
In Amazonis	192.5	29.3	578	thin	4.15	–	–	315.85	177.60	274.62	151.39
Ladon	333.1	−18.2	548.5	thin	–	4.18	–	299.73	166.34	262.18	142.65
CT3-A	181.6	−36.7	538.5	thin	4.17	–	–	294.26	162.56	257.94	139.71
Amenthes	110.6	−0.8	535	thin	4.22	–	–	292.35	161.24	256.46	138.68
Sirenum	205.3	−67.4	534.5	thick	4.20	–	–	296.77	154.11	256.25	138.53
Hematite	357.8	3.2	532.5	thin	4.14	–	–	290.98	160.30	255.40	137.94
Prometheus	93.9	−83.3	462	thick	–	4.04	–	253.29	131.06	225.24	117.41
Huygens	55.6	−13.8	233.5	thin	–	4.00	3.98	127.60	57.20	123.13	54.14
Schiaparelli	16.8	−2.4	222.5	thin	–	3.93	3.92	121.58	53.85	117.99	51.25
Gamma	2.8	−36.7	213.5	thin	–	4.05	–	116.67	51.14	113.75	48.91
Cassini	32.1	23.4	204	thin	–	4.06	4.03	111.48	48.31	109.26	46.44
Antoniadi	60.8	21.4	200	thin	–	3.91	3.79	109.29	47.13	107.36	45.41
epsilon	356.2	−21.6	179	thin	–	4.11	–	97.81	41.03	97.32	40.04
Tikhonravov	35.9	13.3	171.5	thin	–	4.16	4.10	93.72	38.89	93.71	38.14
zeta	283.2	−58.8	170.5	thick	–	3.98	–	85.71	43.30	93.22	37.89
eta	53.2	23.5	170	thin	–	4.18	–	92.90	38.47	92.98	37.77
iota	28.9	−0.3	162.5	thin	–	4.14	–	88.80	36.36	89.34	35.88
Newton	201.9	−40.4	156	thick	–	3.98	4.11	77.82	39.23	86.17	34.26
deVaucouleurs	171.1	−13.2	155.5	thin	–	3.94	3.95	84.97	34.41	85.93	34.13
Copernicus	191.2	−48.8	150.5	thick	–	3.99	4.00	74.84	37.69	83.48	32.89
Herschel	129.9	−14.4	148.5	thick	–	3.92	3.95	73.76	37.14	82.50	32.40

Note. The list of basins, east longitude (long), latitude (lat) and final crater radius ($r_{f(lit)}$) was adapted from Lillis et al. (2013). Average crustal thickness (*ct*) was measured after Goossens et al. (2017) and approximated to thin (closer to 47 km) or thick (closer to 91 km). Transient crater radius ($r_{tc(ss)}$) and impactor size estimates (L_{ss}) based on Π group scaling were calculated using Equations 4 and 7. Coordinates in degrees, ages in Ga, all other values in km. Crater list adapted from Lillis et al. (2013), with model ages from [1]Frey (2008), [2]Robbins et al. (2013) and [3]Werner (2008).
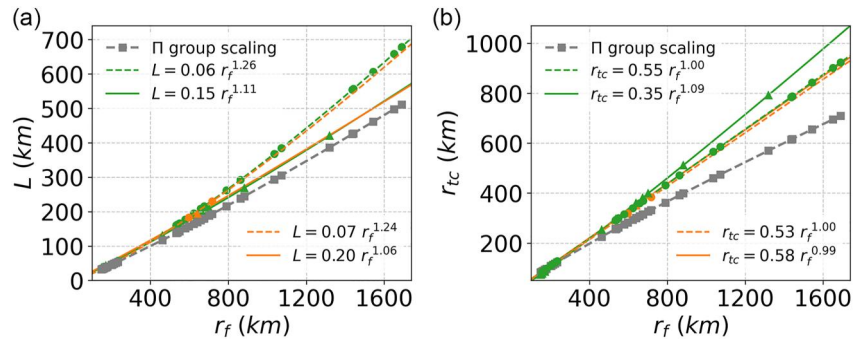
Figure 6. (a) Impactor size (L) and (b) transient crater radius estimates (r_{tc}) for the largest impact basins on Mars listed in Table 1 (markers). Estimates based on Π group scaling (gray squares) were calculated using Equations 4 and 7. Estimates based on our scaling are represented by marker color coded the same as in Figure 1 based on crustal thickness and age. The colored lines show the scaling relationships used for the estimates, recalculated as a function of r_f. Both graphs show a total of 41 projectile size/transient crater radius estimates.

than the ones calculated for a thinner crust. Therefore, it is likely that the temperature is the second most important control of basin final size and morphology after gravity, leaving crustal thickness and temperature in third place.

Our scaling relationships indicate that basins formed in a warmer crust have larger final diameters in comparison to basins formed in a colder crust. This difference is further accentuated as the basin size increases. This result agrees with the work done on lunar impact basins, where the main result demonstrated that impact basins in a "hot" crust may form up to twice the size of impact basins forming in a "cold" crust, for the same impact conditions (Miljkovic et al., 2013). The difference is that for Mars, the discrepancy due to temperature condition isn't that large, with the difference not exceeding more than 10% for craters around 1,200 km in diameter.

As basin size increases, the discrepancy between Π group scaling relationships and the scaling relationships derived from our simulations becomes larger, resulting in significantly different transient crater radius and impactor size estimates at the larger end. One possible explanation is the difference in geomechanical behavior induced by progressively larger portions of the mantle being involved as impacts become larger. As the impacts become larger, the impactor size eventually becomes larger than the thickness of the crust, digging progressively deeper into the mantle. Given that the geomechanical behavior of the mantle is different from that of the crust, it is reasonable to assume that the material displaced by large impacts will behave differently than the material displaced by small impacts, mostly derived from the crust and uppermost mantle.
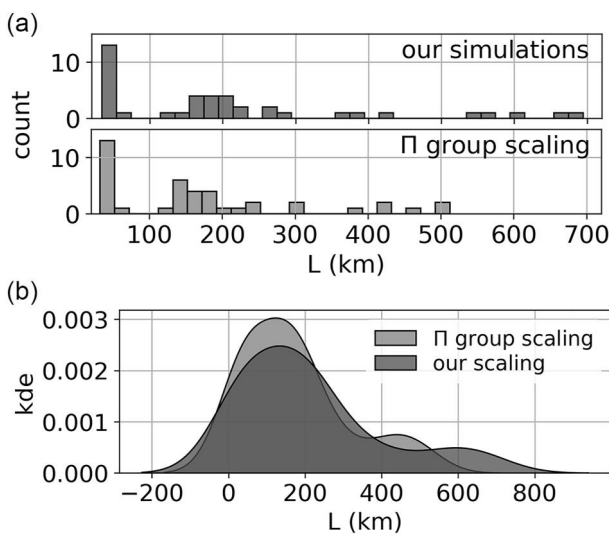
8. Conclusions

We used recent geophysical models (Plesa et al., 2022; Wieczorek et al., 2022) to determine the most suitable target conditions at the time of impact, which were taken as inputs for numerical simulations of large impacts on Mars. Based on our simulation results, we proposed a new set of scaling relationships for Mars basins formed in two crustal thicknesses (47 and 91 km) at three points in time (4.4, 4.0 and 3.5 Ga) and enlisted possible causes for observed divergences in relation to classical scaling. It is likely that all basins formed between 4.4 and 3.5 Ga, making the 3.5 Ga and 4.4 Ga cases end members for the youngest and oldest crust during the basin-forming epoch on Mars.

For the same impact conditions, different temperature profiles and crustal thicknesses resulted in impact basins of different sizes and morphologies. Overall, an impact basin formed in a thin crust presented mantle uplift and crustal thickening radius smaller than the final basin radius. An impact basin forming at 3.5 and 4.0 Ga presented a discernible main rim with smaller mantle uplift and crustal thickening radius. An impact basin forming in a thin

Figure 7. Frequency size distributions of projectile size estimates derived (a) from our simulations (L) and from Π group scaling (L_{ss}), separated in 20 km wide bins. They show 41 estimates for each scenario corresponding to each impact basin listed in Lillis et al. (2013). The estimates are also shown as (b) color coded kernel density distributions.

crust at 4.4 Ga was different, with no distinct topographical features observed and comparatively larger mantle uplift and crustal thickening radius. Impact basins forming in a thick crust presented similar behavior across the investigated ages. The topographical profile was mostly flat with no prominent features. The radius of crustal thickening was larger than the final basin radius, while the radius of mantle uplift was equivalent to approximately 50% of the final basin radius. Mixing between heated crustal and mantle material was observed at the crater center, being largest in volume in older basins.

Our results show that the morphology and size of impact basins on Mars are controlled by age and crustal thickness. Both age and crustal thickness variations imply different temperature profiles. Overall, the temperature is proportional to age, meaning that an old crust is warmer than a young crust. In addition to that, higher crustal thickness values imply higher overall temperatures for the given age. Hence, we can conclude that the temperature is the main control of basin size and morphology on Mars, second only to gravity.

For most ages and crustal thicknesses investigated, Π group scaling slightly overestimated the transient crater radius for craters smaller than 200 km and overestimated it for larger craters. The differences between the Π group scaling and our numerically derived scaling rapidly increased with size, being even more pronounced for a thick crust. For craters with a final radius smaller than 200 km formed in thin crust, Π group scaling reasonably agreed with the scaling derived from our simulations. In all other scenarios, it overestimated the final crater radius, with differences increasing with size. Overall, for a given final radius, Π group scaling underestimates the transient crater radius in comparison to our scaling. This trend is more prominent as crater size increases and is affected by increasing crustal thickness and age.

We used our scaling to estimate impactor sizes for the largest basins on Mars. According to our scaling, the largest basins on Mars were created by impactors ranging from 35 to 680 km in diameter. For the entire size range considered in this study, our scaling predicts larger projectiles for each given basin in comparison to Π group scaling, with differences as high as 32% in impactor diameter. Transient crater radius estimates based on our scaling also diverge from Π group scaling estimates. For basins with a final diameter smaller than 170 km, Π group scaling predicts larger transient crater radii than our scaling. For basins with a larger final diameter, our scaling predicts larger transient crater radii. Overall, this difference increases with the final crater radius.

This extensive numerical modeling work, which encompassed more than 100 numerical simulations totaling hundreds of hours of computing runtime, has opened doors to furthering our understanding of Mars impact basins, their morphology and dependence on the interior structure and thermal state at the time of their formation. Building on this work, we can expand our understanding into the extent of the early and large impact bombardment on Mars, and provide a more comprehensive knowledge of impact basin formation on planetary surfaces.

Data Availability Statement

The temperature profiles shown in Figure 1a and used in our simulations were taken from Plesa et al. (2022). The simulation input files used to generate Figures 1b, 2 and 3, as detailed in *2 Hydrocode simulation setup*, are available at https://zenodo.org/doi/10.5281/zenodo.10100099 (Branco et al., 2023). In Table 1, the list of basins, east longitude, latitude, age, and final crater radius were adapted from Lillis et al. (2013), and the average crustal thickness was measured after Goossens et al. (2017); all other values were calculated by the authors and are available in Table S1. We use the iSALE-2D Dellen release of the iSALE shock physics code (Amsden et al., 1980; Collins et al., 2004; Wünnemann et al., 2006). The iSALE-2D Dellen release is distributed on a case-by-case basis to academic users in the impact community, strictly for non-commercial use. Scientists interested in using or developing iSALE may apply to use it at https://isale-code.github.io/.

References

Amsden, A., Ruppel, H., & Hirt, C. (1980). *SALE: A simplified ALE computer program for fluid flow at all speeds*. Los Alamos National Laboratories Report, LA-8095:101p. Los Alamos, New Mexico. LANL.

Baker, D. M. H. (2016). Updated catalogs of peak-ring basins and Protobasins on Mars [Conference expanded abstract]. 47th Lunar and Planetary Science Conference, Houston, Texas, USA. https://www.hou.usra.edu/meetings/lpsc2016/

Branco, H. C., Katarina, M., & Ana-Catalina, P. (2023). Data from "New numerically derived scaling relationships for impact basins on Mars". *Zenodo*. https://doi.org/10.5281/zenodo.10100099

Bridgman, P. W. (1949). *Dimensional analysis* (p. 113). Yale University Press.

Buckingham, E. (1914). On physically similar systems: Illustrations of the use of dimensional equations. *Physical Review*, *4*, 345–376. https://doi.org/10.1103/physrev.4.345

Collins, G. S. (2014). Numerical simulations of impact crater formation with dilatancy. *Journal of Geophysical Research: Planets*, *119*(12), 2600–2619. https://doi.org/10.1002/2014je004708

Collins, G. S., Melosh, H. J., & Ivanov, B. A. (2004). Modelling damage and deformation in impact simulations. *Meteoritics & Planetary Sciences*, *39*(2), 217–231. https://doi.org/10.1111/j.1945-5100.2004.tb00337.x

Collins, G. S., Melosh, H. J., & Wünnemann, K. (2011). Improvements to the epsilon-alpha compaction model for simulating impacts into high-porosity solar system objects. *International Journal of Impact Engineering*, *38*(6), 434–439. https://doi.org/10.1016/j.ijimpeng.2010.10.013

Collins, G. S., Patel, N., Davison, T. M., Rae, A. S. P., Morgan, J. V., Gulick, S. P. S., et al. (2020). A steeply-inclined trajectory for the Chicxulub impact. *Nature Communications*, *11*(1), 1480. https://doi.org/10.1038/s41467-020-15269-x

Farley, K. A., Malespin, C., Mahaffy, P., Grotzinger, J. P., Vasconcelos, P. M., Milliken, R. E., et al. (2013). In situ radiometric and exposure age dating of the Martian surface. *Science*, *343*(1247166). https://doi.org/10.1126/science.1247166

Frey, H. (2008). Ages of very large impact basins on Mars: Implications for the late heavy bombardment in the inner solar system. *Geophysical Research Letters*, *35*(13), L13203. https://doi.org/10.1029/2008GL033515

Golombek, M., Warner, N. H., Grant, J. A., Hauber, E., Ansan, V., Weitz, C. M., et al. (2020). Geology of the InSight landing site on Mars. *Nature Communications*, *11*(1), 1014. https://doi.org/10.1038/s41467-020-14679-1

Goossens, S., Sabaka, T. J., Genova, A., Mazarico, E., Nicholas, J. B., & Neumann, G. A. (2017). Evidence for a low bulk crustal density for Mars from gravity and topography. *Geophysical Research Letters*, *44*(15), 7686–7694. https://doi.org/10.1002/2017GL074172

Groot, M., Baratoux, D., Hauber, E., Sautter, V., Mustard, J., Gasnault, O., et al. (2013). Long term evolution of the Martian crust-mantle system. *Space Science Reviews*, *174*(49), 111. https://doi.org/10.1007/s11214-012-9948-3

Hirt, C., Claessens, S. J., Kuhn, M., & Featherstone, W. E. (2012). Kilometer-resolution gravity field of Mars: MGM2011. *Planetary and Space Science*, *67*(1), 147–154. https://doi.org/10.1016/j.pss.2012.02.006

Holsapple, K. A. (1987). The scaling of impact phenomena. *International Journal of Impact Engineering*, *5*(1–4), 343–355. https://doi.org/10.1016/0734-743X(87)90051-0

Holsapple, K. A. (1993). The scaling of impact processes in Planetary Sciences. *Annual Review of Earth and Planetary Sciences*, *221*(1), 333–373. https://doi.org/10.1146/annurev.ea.21.050193.002001

Holsapple, K. A., & Schmidt, R. M. (1982). On the scaling of crater dimensions 2: Impact processes. *Journal of Geophysical Research: Planets*, *87*(B3), 1849–1870. https://doi.org/10.1029/JB087iB03p01849

Ivanov, B. (2008). Size-frequency distribution of asteroids and impact craters: Estimates of impact rate. In V. V. Adushkin & I. V. Nemchinov (Eds.), *Catastrophic events caused by Cosmic objects* (pp. 91–116). Springer.

Ivanov, B. A., Deniem, D., & Neukum, G. (1997). Implementation of dynamic strength models into 2D hydrocodes: Applications for atmospheric breakup and impact cratering. *International Journal of Impact Engineering*, *20*(1–5), 411–430. https://doi.org/10.1016/s0734-743x(97)87511-2

Ivanov, B. A., Melosh, H. J., & Pierazzo, E. (2010). Basin-forming impacts: Reconnaissance modeling. In R. L. Gibson & W. U. Reimold (Eds.), *Large meteorite impacts and planetary evolution IV* (Vol. 465, pp. 29–49). Geological Society of America Special Paper. https://doi.org/10.1130/2010.2465(03

Johnson, B. C., Blair, D. M., Collins, G. S., Melosh, H. J., Freed, A. M., Taylor, G. J., et al. (2016). Formation of the Orientale lunar multiring basin. *Science*, *154*(6311), 441–444. https://doi.org/10.1126/science.aag0519

Johnson, B. C., Milliken, R. E., Lewis, K. W., & Collins, G. S. (2021). Impact generated porosity in Gale crater and implications for the density of sedimentary rocks in lower Aeolis Mons. *Icarus*, *366*(114539), 114539. https://doi.org/10.1016/j.icarus.2021.114539

Johnson, C. L., Mittelholz, A., Langlais, B., Russell, C. T., Ansan, V., Banfield, D., et al. (2020). Crustal and time-varying magnetic fields at the InSight landing site on Mars. *Nature Geoscience*, *13*(3), 199–204. https://doi.org/10.1038/s41561-020-0537-x

Knapmeyer-Endrun, B., Panning, M. P., Bissig, F., Joshi, R., Khan, A., Kim, D., et al. (2021). Thichness and structure of the Martian crust from InSight seismic data. *Science*, *373*(6553), 438–443. https://doi.org/10.1126/science.abf8966

Le Feuvre, M., & Wieczorek, M. A. (2011). Nonuniform cratering of the Moon and and a revised crater chronology of the inner Solar System. *Icarus*, *2014*, 1–20. https://doi.org/10.1016/j.icarus.2011.03.010

Li, J., Beghein, C., McLennan, S. M., Horleston, A. C., Charalambous, C., Huang, Q., et al. (2022). Constraints on the Martian crust away from the InSight landing site. *Nature Communications*, *13*(1), 7950. https://doi.org/10.1038/s41467-022-35662-y

Lillis, R., Robbins, S., Manga, M., Halekas, J. S., & Frey, H. V. (2013). Time history of the Martian dynamo from crater magnetic field analysis. *Journal of Geophysical Research: Planets*, *118*(7), 1488–1511. https://doi.org/10.1002/jgre.20105

Lognonné, P., Banerdt, W. B., Pike, W. T., Giardini, D., Christensen, U., Garcia, R. F., et al. (2020). Constraints on the shallow elastic and anelastic structure of Mars from InSight seismic data. *Nature Geoscience*, *13*(3), 213–220. https://doi.org/10.1038/s41561-020-0536-y

Manske, L., Marchi, S., Plesa, A. C., & Wunnemann, K. (2021). Impact melting upon basin formation on early Mars. *Icarus*, *357*(114118), 114128. https://doi.org/10.1016/j.icarus.2020.114128

Marchi, S. (2021). A new Martian crater chronology: Implications for Jezero Crater. *The Astronomical Journal*, *161*(4), 187. https://doi.org/10.3847/1538-3881/abe417

Melosh, H. J. (1989). *Impact cratering, A geologic process*. Oxford University Press.

Melosh, H. J. (1997). Acoustic fluidization: A new geologic process? *Journal of Geophysical Research*, *84*(B13), 7513–7520. https://doi.org/10.1029/jb084ib13p07513

Melosh, H. J. (2011). *Planetary surface processes*. Cambridge University Press.

Melosh, H. J., Freed, A. M., Johnson, B. C., Blair, D. M., Andrews-Hanna, J. C., Neumann, G. A., et al. (2013). The origin of lunar mascon basins. *Science*, *340*(6140), 1552–1555. https://doi.org/10.1126/science.1235768

Melosh, H. J., Ryan, E. V., & Asphaug, E. (1992). Dynamic fragmentation in impacts: Hydrocode simulation of laboratory impacts. *Journal of Geophysical Research*, *97*(E9), 14735–14759. https://doi.org/10.1029/92je01632

Miljkovic, K., Collins, G. S., Wieczorek, M. A., Soderblom, J. M., Neumann, G. A., & Zuber, M. T. (2016). Subsurface morphology and scaling of lunar impact basins. *Journal of Geophysical Research: Planets*, *121*(9), 1695–1712. https://doi.org/10.1002/2016JE005038

Miljkovic, K., Wieczorek, M. A., Collins, G. S., Laneuville, M., Neumann, G. A., Melosh, H. J., et al. (2013). Asymmetric distribution of lunar impact basins caused by variations in target properties. *Science*, *343*(6159), 724–726. https://doi.org/10.1126/science

Miljkovic, K., Wieczorek, M. A., Collins, G. S., Solomon, S. C., Smith, D. E., & Zuber, M. T. (2015). Excavation of the lunar mantle by basin-forming impact events on the Moon. *Earth and Planetary Science Letters*, *409*, 243–251. https://doi.org/10.1016/j.epsl.2014.10.041

Miljkovic, K., Wieczorek, M. A., Laneuville, M., Nemchin, A., Bland, P. A., & Zuber, M. T. (2021). Large impact cratering during lunar magma ocean solidification. *Nature Communications*, *12*(1), 5433. https://doi.org/10.1029/2004JE002262

Ohnaka, M. (1995). A shear failure strength law of rock in the brittle-plastic transition regime. *Geophysical Research Letters*, *22*(1), 25–28. https://doi.org/10.1029/94gl02791

Osinski, G. R., & Pierazzo, E. (2013). *Impact cratering: Processes and products*. Blackwell Publishing Ltd.

Pierazzo, R., & Melosh, H. J. (2000). Hydrocode modeling of oblique impacts: The fate of the projectile. *Meteoritics & Planetary Sciences*, *25*(1), 117–130. https://doi.org/10.1111/j.1945-5100.2000.tb01979.x

Plesa, A. C., Padovan, S., Tosi, N., Breuer, D., Grott, M., Wieczorek, M. A., et al. (2018). The thermal state and interior structure of Mars. *Geophysical Research Letters*, *45*(22), 12198–12209. https://doi.org/10.1029/2018GL080728

Plesa, A. C., Wieczorek, M., Knapmeyer, M., Rivoldini, A., Walterová, M., & Breuer, D. (2022). Interior dynamics and thermal evolution of Mars - A geodynamic perspective. In C. Schmelzbach & S. C. Stähler (Eds.), *Advances in geophysics: Geophysical exploration of the solar system* (Vol. 63).

Potter, R. W. K. (2011). *Numerical modelling of basin-scale impact crater formation* (Doctoral thesis). Imperial College London.

Potter, R. W. K. (2015). Investigating the onset of multi-ring impact basin formation. *Icarus*, *261*, 91–99. https://doi.org/10.1016/j.icarus.2015.08.009

Potter, R. W. K., Collins, G. S., Kiefer, W. S., McGovern, P. J., & Kring, D. A. (2012). Constraining the size of the South Pole-Aitken basin impact. *Icarus*, *220*(2), 730–743. https://doi.org/10.1016/j.icarus.2012.05.032

Potter, R. W. K., Kring, D. A., Collins, G. S., Kiefer, W. S., & McGovern, P. J. (2012). Estimating transient crater size using the crustal annular bulge: Insights from numerical modeling of lunar basin-scale impacts. *Geophysical Research Letters*, *29*(18), L18203. https://doi.org/10.1029/2012GL052981

Robbins, J. S., Hynek, B. M., Lillis, R. J., & Bottke, W. F. (2013). Large impact crater histories of Mars: The effect of different model crater age techniques. *Icarus*, *225*(1), 173–184. https://doi.org/10.1016/j.icarus.2013.03.019

Robbins, S. J., & Hynek, B. M. (2012). A new global database of Mars impact craters ≥1 km: 2. Global crater properties and regional variations of the simple-to-complex transition diameter. *Journal of Geophysical Research*, *117*(E6), E06001. https://doi.org/10.1029/2011JE003967

Stähler, S. C., Khan, A., Banerdt, W. B., Lognonné, P., Giardini, D., Ceylan, S., et al. (2021). Seismic detection of the martian core. *Science*, *373*(6553), 443–448. https://doi.org/10.1126/science.abi7730

Thompson, S., & Lauson, H. (1972). Improvements in the CHART D radiation-hydrodynamic code III: Revised analytic equations of state. Sandia National Laboratory Report, SC-RR-71 0714 (p. 113).

Trowbridge, A. J. (2020). *From the Moon to Pluto: The use of impact and convection modeling as a window into planetary interiors* (PhD thesis). Purdue University, Department of Earth, Atmospheric and Planetary Sciences.

Werner, S. C. (2008). The early Martian evolution - Constraints from basin formation ages. *Icarus*, *195*(1), 45–60. https://doi.org/10.1016/j.icarus.2007.12.008

Werner, S. C. (2014). Moon, Mars, Mercury: Basin formation ages and implications for the maximum surface age and the migration of gaseous planets. *Earth and Planetary Science Letters*, *400*, 54–65. https://doi.org/10.1016/j.epsl.2014.05.019

Werner, S. C. (2019). In situ calibration of the Martian cratering chronology. *Meteoritics & Planetary Sciences*, *54*(5), 1182–1193. https://doi.org/10.1111/maps.13263

Werner, S. C., Tanaka, K. L., & Skinner, J. A., Jr. (2011). Mars: The evolutionary history of the northern lowlands based on crater counting and geologic mapping. *Planetary and Space Science*, *59*(11–12), 1143–1165. https://doi.org/10.1016/j.pss.2011.03.022

Wieczorek, M. A., Broquet, A., McLennan, S. M., Rivoldini, A., Golombek, M., Antonangeli, D., et al. (2022). InSight constrains on the global character of the Martian crust. *Journal of Geophysical Research: Planets*, *127*(5), e2022JE007298. https://doi.org/10.1029/2022JE0072

Wünnemann, K., Collins, G., & Melosh, H. (2006). A strain-based porosity model for use in hydrocode simulations of impacts and implications for transient crater growth in porous targets. *Icarus*, *180*(2), 514–527. https://doi.org/10.1016/j.icarus.2005.10.013